Neutron-rich rare-isotope production from projectile fission of heavy nuclei near 20 MeV/nucleon beam energy

N. Vonta,[1,2] G. A. Souliotis,[1,*] W. Loveland,[3] Y. K. Kwon,[2] K. Tshoo,[2] S. C. Jeong,[2] M. Veselsky,[4] A. Bonasera,[5,6] and A. Botvina[7,8]

[1]*Laboratory of Physical Chemistry, Department of Chemistry, National and Kapodistrian University of Athens, Athens 15771, Greece*
[2]*Rare Isotope Science Project (RISP), Institute for Basic Science, Daejeon 305-811, Korea*
[3]*Department of Chemistry, Oregon State University, Corvallis, Oregon 97331, USA*
[4]*Institute of Physics, Slovak Academy of Sciences, Bratislava 84511, Slovakia*
[5]*Cyclotron Institute, Texas A&M University, College Station, Texas 77843, USA*
[6]*Laboratori Nazionali del Sud, INFN, via Santa Sofia 62, I-95123 Catania, Italy*
[7]*Frankfurt Institute for Advanced Studies, Goethe University, D-60438 Frankfurt am Main, Germany*
[8]*Institute for Nuclear Research, Russian Academy of Sciences, RU-117312 Moscow, Russia*

(Received 24 August 2016; revised manuscript received 28 October 2016; published 19 December 2016)

We investigate the possibilities of producing neutron-rich nuclides in projectile fission of heavy beams in the energy range of 20 MeV/nucleon expected from low-energy facilities. We report our efforts to theoretically describe the reaction mechanism of projectile fission following a multinucleon transfer collision at this energy range. Our calculations are mainly based on a two-step approach: The dynamical stage of the collision is described with either the phenomenological deep-inelastic transfer model (DIT) or with the microscopic constrained molecular dynamics model (CoMD). The de-excitation or fission of the hot heavy projectile fragments is performed with the statistical multifragmentation model (SMM). We compared our model calculations with our previous experimental projectile-fission data of ^{238}U (20 MeV/nucleon) + ^{208}Pb and ^{197}Au (20 MeV/nucleon) + ^{197}Au and found an overall reasonable agreement. Our study suggests that projectile fission following peripheral heavy-ion collisions at this energy range offers an effective route to access very neutron-rich rare isotopes toward and beyond the astrophysical r-process path.

DOI: 10.1103/PhysRevC.94.064611

I. INTRODUCTION

The study of the nuclear landscape toward the astrophysical r-process path and the neutron dripline is presently of special importance to the nuclear physics and astrophysics community (see, e.g., Refs. [1–3] and references therein). Closely related to this study is the efficient production of very neutron-rich nuclides, which is a central issue in current and future rare isotope beam facilities (see, e.g., Refs. [4–15]).

Neutron-rich nuclides are mainly produced by spallation, fission, and projectile fragmentation [16]. Spallation is an efficient mechanism to produce rare isotopes for ISOL-type techniques [17,18]. High-energy projectile fission is appropriate in the region of light and heavy fission fragments (see, e.g., Refs. [19–22] for recent efforts on ^{238}U projectile fission). Finally, projectile fragmentation offers a universal approach to produce exotic nuclei at beam energies typically above 100 MeV/nucleon (see, e.g., Refs. [23–30]). In addition to the above methods, peripheral reactions from the Coulomb barrier [31–35] to the Fermi energy (20–40 MeV/nucleon) [36] have been shown to produce very neutron-rich nuclei. Such reactions offer the possibility of picking up a number of neutrons from the target, in addition to the stripping of protons. In this respect, we report in Ref. [37] a computational description of the reaction mechanism for near projectile fragments and give insight on the theoretical understanding of very neutron-rich isotope production to which substantial experimental effort has been devoted by us in recent years [36,38–41].

Motivated by recent developments in several facilities that will produce intense heavy beams [7,10,11,14] in the energy range 15–25 MeV/nucleon, we intend to investigate the possibilities of producing neutron-rich rare isotopes employing projectile fission following multinucleon transfer in this energy range. In this article, we will refer to this approach as quasiprojectile (QP) fission or, simply, projectile fission. The mechanism is essentially fission of a heavy quasiprojectile that results from extensive multinucleon transfer in the interaction of the projectile with a heavy target. As is the case for reactions with lighter nonfissionable projectiles [36,37] in this energy range, the QP fission approach offers the advantage of very broad N/Z distributions of the primary heavy QP that undergoes fission, thus leading to extremely (and possibly new) neutron-rich fission fragments. Moreover, the velocities of the projectile fission fragments can be high enough to allow adequate in-flight collection and separation in appropriate large acceptance separators.

Projectile fission in the Fermi energy range was studied by us some years ago with a 20-MeV/nucleon ^{238}U beam interacting with a ^{208}Pb target [42,43]. In addition, projectile fission data of a 20-MeV/nucleon ^{197}Au beam were also obtained as part of an extensive study of Au-induced reactions [44,45].

In this paper, we present a theoretical analysis of our previous experimental projectile-fission data of the 20-MeV/nucleon reactions ^{238}U + ^{208}Pb [42] and

*Corresponding author: soulioti@chem.uoa.gr

^{197}Au + ^{197}Au [45]. A short description of the experimental method and data collection is also given. In the present work, the dynamical calculations are performed with either the phenomenological deep-inelastic transfer model (DIT) [46], or with the microscopic constrained molecular dynamics model (CoMD) [47]. The de-excitation (including fission) of the hot heavy projectile fragments is performed with the statistical multifragmentation model (SMM) [48,49]. Furthermore, microscopic calculations with CoMD that follow the complete reaction dynamics will also be presented following the developments reported in our recent article [50].

We will show that the present model framework is able to adequately describe the experimental data and, furthermore, may allow dependable predictions of rates of neutron-rich rare isotopes in various production and separation schemes employing the projectile fission approach. This latter possibility is crucial for the selection and design of the proper separator configuration and the optimum projectile and target combination (as well as the appropriate target thickness) for efficient production, collection, and separation of very neutron-rich nuclei from projectile fission.

The structure of the paper is as follows. In Sec. II, a short overview of our previous experimental measurements of projectile fission at 20 MeV/nucleon is given. In Sec. III, a description of the theoretical models is presented, followed, in Sec. IV, by a systematic comparison of the calculations with the experimental data. In Sec. V, a summary and conclusions are given. Finally, in Appendix A, the target and energy dependence of fission-fragment cross sections are presented and, in Appendix B, the properties of the primary quasiprojectiles are discussed.

II. OUTLINE OF THE EXPERIMENTAL METHODS AND DATA

Before presenting the theoretical models and comparisons to data, a brief description of the experimental approach and data analysis is given for completeness. The experimental data on 20 MeV/nucleon ^{238}U and ^{197}Au projectile fission were obtained at the National Superconducting Cyclotron Laboratory (NSCL) of Michigan State University using the A1200 fragment separator [51]. The use of the A1200 for the production and identification of medium and heavy mass fragments has been discussed in detail in Refs. [44,45]. Herein, we briefly summarize the experimental setup and procedures. The A1200 spectrometer was operated in the medium acceptance mode with an angular acceptance $\Delta\Omega = 0.8$ msr ($\Delta\theta = 20$ mr, $\Delta\phi = 40$ mr) and a momentum acceptance $\Delta p/p = 3\%$. In this mode, the A1200 provided two intermediate dispersive images and a final achromatic image (focal plane).

For the U+Pb data, a 20-MeV/nucleon ^{238}U^{35+} beam with current 0.05-particle nA (3.1×10^8 particles/s) struck a target of ^{208}Pb (5.8 mg/cm^2, 99.1% enriched) at the object position of A1200 at an angle of 1° relative to the optical axis of the spectrometer. Fission fragments from the decay of the projectile, arriving at the first dispersive image of the spectrometer, passed through a slit defining a 3% momentum acceptance and an X-Y position-sensitive parallel-plate avalanche counter (PPAC) [52] giving a start timing signal. The horizontal position of this PPAC, along with NMR measurements of the dipole magnetic field, were used to determine the magnetic rigidity of the particles. At the focal plane, 14 m from the PPAC detector, the fragments passed through a second PPAC giving a stop timing signal and then entered into a four-element (50, 50, 300, and 500 μm) Si detector telescope.

For each event, time of flight, energy loss, residual energy, and magnetic rigidity were recorded. The spectrometer and the detectors were calibrated using a low-intensity ^{238}U beam and a series of analog beams. From the measured quantities, the atomic number Z, the velocity υ, the ionic charge q, the mass number A, and the magnetic rigidity $B\rho$ were obtained for each event. Further details of the procedure are reported in Refs. [44,45]. Here we briefly mention that the determination of the atomic number Z was based on the energy loss ΔE_1 and ΔE_2 of the particles in the Si detectors [53,54] and their velocity, with resolution (FWHM) of 0.5 Z units. The ionic charge q of the particles exiting the target was obtained from the total energy $E_{\rm tot} = \Delta E_1 + \Delta E_2 + \mathrm{E}_r$ (the last term being the energy in the stopping Si detector), the velocity υ, and the magnetic rigidity via the magnetic rigidity equation $B\rho = p/q$ (where p is the momentum). The resulting ionic charge q had a resolution of 0.4 units (FWHM). Since q must be an integer, we assigned integer values of q for each event by setting windows ($\Delta q = 0.4$) on each peak of the q spectrum at each magnetic rigidity setting of the spectrometer. Using the $B\rho$ and the velocity measurements, the mass-to-charge A/q ratio of each ion was calculated from the magnetic rigidity equation. Finally, combining the q determination with the A/q measurement, the mass number A was obtained as

$$A = q_{\rm int} \times A/q \tag{1}$$

($q_{\rm int}$ is the integer ionic charge determined as described above) with an overall resolution (FWHM) of about 0.7 A units. To cover the mass and velocity range of the fission fragments, data were taken at several overlapping $B\rho$ settings of the spectrometer in the range 1.7–2.0 Tm. These settings were such that only fission fragments emitted forward in the rest frame of the quasiprojectile fissioning nucleus were accepted by the spectrometer.

To obtain production cross sections, the observed counts were normalized to the beam current and target thickness and, furthermore, were corrected for the yields of charge states missed by the focal plane detectors due to charge changing of the ions passing through the PPAC at the first image of the A1200. These corrections were based on the ionic charge distribution data of Leon *et al.* [55] and were typically factors of 2–4. Furthermore, the yields were corrected for the limited angular acceptance of the spectrometer. For this correction, the angular distribution of the fission fragments was assumed to arise from an isotropic emission in the frame of the fissioning nucleus taken to be the projectile deflected on average at an angle equal to the grazing angle $\theta_{gr} \sim 10^o$ of the U+Pb reaction [56].

The Au+Au data were obtained under similar conditions as the U+Pb data, as part of our study of Au-induced reactions on heavy targets [45], which followed our studies of Au+C,

Al reactions [44]. We note that the Au+Au data were only recently fully analyzed for the purpose of the present work and shown in this article. For these data, a beam of ^{197}Au^{29+} (20 MeV/nucleon) with current 0.5 particle nA (3.1×10^9 particles/s) interacted with a 2 mg/cm^2 ^{197}Au target and forward-moving fission fragments were collected in the $B\rho$ range 1.4–1.8 Tm. We point out that while a beam of ^{197}Au ($N/Z = 2.49$) is not the optimum choice, compared to the ^{238}U ($N/Z = 2.59$) beam, for the production of neutron-rich isotopes, the Au projectile fission data can serve as a complement of the U data for the detailed testing of our model framework, as will be discussed in the following.

III. BRIEF DESCRIPTION OF THE THEORETICAL MODELS

The calculations on projectile fission performed in this work are based on the two-stage approach typically employed for heavy-ion collisions. The dynamical stage of the collision was described with two models: the phenomenological deep-inelastic transfer (DIT) model and the microscopic constrained molecular dynamics (CoMD) model. For peripheral and semiperipheral collisions, the dynamical stage of the collision leads to an excited heavy projectilelike fragment (quasiprojectile) and an excited targetlike fragment (quasitarget). In the second stage, the excited quasiprojectile was de-excited with the statistical multifragmentation model (SMM) in which fission was properly taken into account. Furthermore, a complete dynamical description of the projectile-target interaction was attempted with the CoMD model, along the lines of our recent work on proton-induced fission [50]. We briefly describe the above dynamical and statistical codes and the calculation procedures in the following.

A. The deep-inelastic transfer (DIT) model

The deep-inelastic transfer (DIT) model of Tassan-Got [46] is a phenomenological model that simulates stochastic nucleon exchange in peripheral and semiperipheral collisions. The projectile and the target, assumed to be spherical, approach each other along Coulomb trajectories until they reach the range of the nuclear interaction. At this point the system is represented as two Fermi gases in contact. A window opens in the internuclear potential and nucleons are exchanged stochastically. The direction and type of transfer are chosen by random drawing based on transfer probabilities. The transfer probabilities are calculated via a phase-space integral that involves a phase-space flux term, the barrier penetrability, and the occupation probabilities. The nucleon transfer leads to a variation in mass, charge, excitation energy, and spin of the interacting nuclei. After interaction, the quasiprojectile and the quasitarget are excited and move along Coulomb trajectories. In the DIT model, the exchange of nucleons is assumed to be the only source of energy dissipation. Nucleon-nucleon collisions (mostly blocked by the Pauli principle for low-energy collisions) are not taken into account. The calculations are performed for a wide range of impact parameters from very peripheral to semiperipheral collisions. More specifically, the minimum impact parameter is assumed to be such that the interpenetration of the projectile and target surfaces does not exceed 3 fm [46], at which point the DIT calculation ends. For the case of ^{238}U (20 MeV/nucleon) + ^{208}Pb, the minimum impact parameter is 7 fm [see Fig. 8(c) in Appendix B].

The DIT model has been employed for the description of multinucleon transfer products from our 15- and 25-MeV/nucleon ^{86}Kr-induced reactions [36–39]. Moreover, it has been successfully used in a number of other studies at Fermi energies (e.g., Refs. [57–62]) and is able to describe correctly the N/Z, the excitation energy and kinematical properties of excited projectilelike (and targetlike) residues emerging after the peripheral heavy-ion collision.

B. The constrained molecular dynamics (CoMD) model

The constrained molecular dynamics (CoMD) model is a microscopic model designed for reaction-dynamics studies near and below the Fermi energy [47,63]. Following the approach of quantum molecular dynamics (QMD) models [64], in the CoMD code, nucleons are described as localized Gaussian wave packets. The wave function of the nuclear system is assumed to be the product of these single-particle wave functions. With this Gaussian description, the N-body time-dependent dinger equation leads to (classical) Hamilton's equations of motion for the centroids of the nucleon wave packets. The potential part of the Hamiltonian consists of a simplified Skyrme-like effective interaction and a surface term. The isoscalar part of the effective interaction corresponds to a nuclear matter compressibility of $K = 200$ (soft EOS). For the isovector part, several forms of the density dependence of the nucleon-nucleon symmetry potential are implemented in the code. Two of them were used in the present work, which we named as the standard potential and the soft potential. These forms correspond to a symmetry potential proportional to the density and its square root, respectively (see Ref. [65] and references therein). We note that in the CoMD model, while not explicitly implementing antisymmetrization of the N-body wave function, a constraint in the phase space occupation for each nucleon is imposed, restoring the Pauli principle at each time step of the system evolution. This constraint restores in an approximate way the fermionic nature of the nucleon motion in the interacting nuclei. The short-range (repulsive) nucleon-nucleon interactions are described as individual nucleon-nucleon collisions governed by the nucleon-nucleon scattering cross section, the available phase space, and the Pauli principle, as usually implemented in transport codes.

In the present work, the CoMD code with its standard parameters was used. The soft density-dependent isoscalar potential was used (corresponding to a compressibility $K = 200$ for symmetric nuclear matter). The calculations were performed with both the standard and the soft symmetry potential and lead to nearly identical results. Thus, results with only the standard symmetry potential will be presented in the following figures.

The ground-state configurations of the projectile and the target nuclei were obtained with a simulated annealing approach and were tested for stability for relatively long times (1500–2000 fm/c). These configurations were used in the CoMD code for the subsequent collision simulations.

As with the DIT model, the CoMD calculations for the dynamical stage of the projectile–target interaction were performed in a wide range of impact parameters, following a triangular distribution, covering from peripheral to semiperipheral collisions. The CoMD calculations were terminated at $t = 300$ fm/c and the characteristics of the produced excited quasiprojectiles were determined with the fragment-recognition routine of CoMD. This routine is based on the minimum spanning tree method assuming that nucleons with a relative distance of less than 2.4 fm belong to the same fragment. In the calculations, the excitation energy of the quasiprojectiles was obtained from the difference of their binding energy as given by the CoMD calculation at $t = 300$ fm/c and the corresponding binding energies of the ground-state nuclei taken from mass tables [66].

C. Model for the de-excitation stage

To describe the de-excitation of the hot heavy quasiprojectiles emerging from the dynamical stage, we used the latest version of the statistical multifragmentation model [48,49,67–69]. The SMM model assumes statistical equilibrium at a low-density freeze-out stage and includes all breakup channels ranging from the compound nucleus to vaporization (i.e., channels with only light particles $A < 4$), allowing a unified description of nuclear disintegration from low to high excitation energy. In the microcanonical treatment, the statistical weight of a decay channel is calculated as exponential of the entropy. Light fragments with $A < 4$ are considered as stable particles (nuclear gas) with only translational degrees of freedom. Fragments with $A > 4$ are treated as heated liquid drops with free energies parameterized as a sum of volume, surface, and Coulomb and symmetry energy terms [49] with parameters adopted from the Bethe-Weizsacker mass formula. The model generates a Markov chain of partitions (with the METROPOLIS algorithm) representative of the whole partition ensemble. In the low-density freeze-out configuration, the hot primary fragments are assumed to be isolated and at normal density; they, subsequently, propagate in their mutual Coulomb field, while undergoing binary de-excitation via evaporation, fission, or Fermi breakup [48].

The Coulomb interaction energy is directly calculated for each spatial configuration of fragments in the freeze-out volume. Finally, the effect of the Coulomb field of the target in proximity to the decaying quasiprojectile is included. The evolution of the symmetry energy is taken into account in the mass calculation of primary and secondary fragments as in Refs. [67,68]. Below a threshold of excitation energy per nucleon $\epsilon^* = 1$ MeV, a smooth transition to standard experimental masses is assumed [67]. In the present calculations, the freeze-out density is assumed to be 1/3 of the normal nuclear matter density.

We note that for the de-excitation of low energy ($\epsilon^* < 1.0$ MeV/nucleon) non-fissionable nuclei (relevant for the production of neutron-rich isotopes [37,62]), the SMM code has been shown to adequately describe the particle de-excitation process as a cascade of emissions of neutrons and light charged particles using the Weisskopf-Ewing model of statistical evaporation. In regards to fission of heavier excited nuclei [69], the following approach is followed. A so-called multifragmentation threshold value of $\epsilon^*_{\rm mult} = 0.2$ MeV/nucleon is defined, above which the SMM statistical multipartition is applied, as described above. This threshold value is, of course, much lower than the true nuclear multifragmentation threshold of 2–3 MeV/nucleon, but it is employed in this work as a parameter to define when the SMM multipartition scheme will be applied to the decay of the excited nuclear system. Thus, for intermediate and high excitation energies ($\epsilon^* > \epsilon^*_{\rm mult}$), fission is simply described as a special case of multifragmentation, i.e., the binary partition of the excited heavy nucleus. However, at low excitation energy($\epsilon^* < \epsilon^*_{\rm mult}$), the fission channel is described in the spirit of the liquid-drop model with deformation-dependent shell effects. In the present version of SMM, the Bohr-Wheeler approach [70] is used for the calculation of the partial fission width. The fission barrier is determined as in Myers and Swiatecki [71], and the results of Ref. [72] are used for the level density at the saddle point. The method for obtaining fission mass distributions in the SMM model is described in detail in Ref. [69]. We briefly mention that along with a symmetric fission mode, two asymmetric fission modes are included with contributions dependent on the fissioning nucleus and the excitation energy. These contributions, essentially corresponding to the traditional Brosa modes [73], are described by an empirical parametrization based on analysis of a large body of experimental data [69]. In closing, we point out that the current version of SMM, as described above, can adequately cover the conventional evaporation and fission processes occurring at low excitation energy (i.e., compound-nucleus de-excitation), as well as the transition toward the higher energy multifragmentation regime. In this regime, the binary (fissionlike) partitions of the excited heavy nuclei appear as a class of multifragmentation channels competing with each other according to their statistical weight.

In the present work, apart from the value of $\epsilon^*_{\rm mult} = 0.2$ MeV/nucleon that we used in the calculations presented in the following, we also tested the values 0.5, 1.0, and 1.5 MeV/nucleon, and we concluded that the choice of the low value of 0.2 MeV/nucleon is the optimum for the SMM description of the neutron-rich projectile fission fragments from the studied reactions.

D. Full CoMD description of quasiprojectile fission

Apart from the two-step description using the approaches described above, we also employed the microscopic CoMD code in a standalone mode to perform calculations of the complete dynamics of the reaction following the evolution for long times, up to t = 15 000 fm/c (5.0×10^{-20} s). This CoMD calculation follows our procedures developed in Ref. [50] for the description of proton-induced fission of actinides. For the present work, for a given reaction, a total of 1000 events were collected. For each event the impact parameter of the collision was chosen in the range $b = 0$–13 fm, following a triangular distribution. The phase-space coordinates were registered every 100 fm/c. At each time step, fragments were recognized and their properties were reported. From this information, we followed the evolution of the fissioning

quasiprojectiles and we obtained the properties of the resulting projectile fission fragments. As in Ref. [50], we consider as fission time ($t_{\rm fission}$) for the quasiprojectile, the time interval between the projectile-target contact, and the emergence of two fission fragments from the quasiprojectile. Typical values of $t_{\rm fission}$ are in the range 2000–4000 fm/c. Furthemore, we allowed an additional time $t_{\rm decay} = 5000$ fm/c after scission for the nascent projectile fission fragments to de-excite.

IV. COMPARISON OF MODEL CALCULATIONS WITH DATA

In this section we present a systematic comparison of the calculations on projectile fission fragments from the 20-MeV/nucleon reactions ^{238}U + ^{208}Pb and ^{197}Au + ^{197}Au employing the model framework described above with the experimental data, as discussed in Sec. II.

A. Mass yield and N/Z distributions

In Fig. 1, the isobaric yield distributions (cross sections) of projectile fission fragments from the reaction ^{238}U (20 MeV/nucleon) + ^{208}Pb are presented. The measured cross sections (within the spectrometer acceptance) are shown by the full (black) points. The open points (upper yield curve) are the total cross sections extracted after correction for the acceptance of the spectrometer [42], as also explained in Sec. II. We note

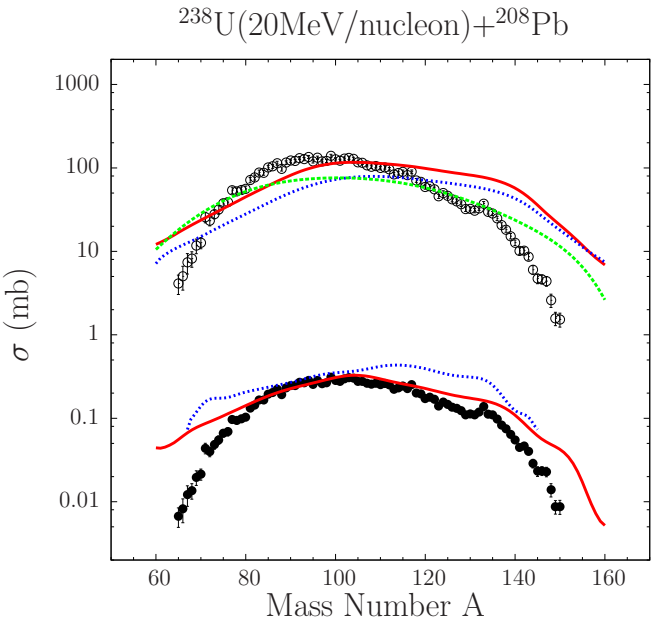

FIG. 1. Isobaric yield distributions (cross sections) of projectile fission fragments from the reaction ^{238}U (20 MeV/nucleon) + ^{208}Pb. Closed points, measured cross sections; open points, total cross sections extracted after correction for the angular acceptance of the spectrometer [42]. Solid (red) lines: DIT/SMM calculations. Dotted (blue) lines CoMD/SMM calculations. The upper set of lines gives total cross sections. The lower set of lines is after filtering with the acceptance of the spectrometer (see text). The dashed (green) line gives the total cross sections from the CoMD calculation of the full dynamics (1000 events, $t = 15\,000$ fm/c).

that the symmetric shape of the measured yield curve rules out any significant contribution of the low-energy fission processes in the reaction mechanism (that, as well known, would lead to asymmetric fission due to shell effects). The solid (red) lines are the results of the DIT/SMM calculations, whereas the dotted (blue) lines are the CoMD/SMM calculations. The upper curves give the total cross sections. The lower curves are obtained after filtering of the corresponding calculations with the angular and $B\rho$ acceptance of the spectrometer.

From the figure, we see some agreement of the calculated isobaric yields with the corrected data, mainly in the central region of the yield curve. The DIT/SMM calculation appears to describe the peak of the mass yield distribution, but it is wider than the measured distribution. We may interpret this as a possible incomplete collection of the heavier fission fragments in the spectrometer due to $B\rho$ coverage. (We point out that collection of fission fragments was possible only when intense scattering of ^{238}U primary beam at various charge states was not present.)

Furthermore, we compare the filtered calculated isobaric yields with the measured data and we see an agreement again mainly in the central region of the yield curve. This provides confidence in our overall model framework regarding a realistic description of not only the yields of the fission fragments but also their kinematical properties and the ionic charge state distributions. In our calculations, the ionic charge states of the fragments have been simulated in a Monte Carlo fashion following the Gaussian parametrizations given in Ref. [55].

Finally, the dashed (green) line is a complete CoMD calculation (1000 events, $t = 15\,000$ fm/c) of projectile fission fragments and is in reasonable agreement with the two-step calculations as well as the data. We note that due to the relatively low statistics of this calculation, filtering of the events with the spectrometer acceptance was not performed (thus, a corresponding filtered mass yield curve is not shown in Fig. 1).

In Fig. 2, we present the average Z/A (proton fraction) versus A of projectile fission fragments from the reaction ^{238}U (20 MeV/nucleon) + ^{208}Pb. The experimental data are given by the closed points [42]. The full (red) lines are calculations with DIT/SMM. The dotted (blue) lines are calculations with CoMD/SMM. The continuous (black) line gives the line of β stability. The upper set of calculated curves are the final (cold) fragments produced after de-excitation of the primary (hot) fragments obtained at the partition stage of SMM. The average Z/A of these hot fragments is given by the lower set of curves. We observe that the DIT/SMM and CoMD/SMM calculations for the fission fragments are on average less neutron rich that experimental data. As we will also discuss in the following regarding Figs 3 and 4, we understand that the experimental data did not cover a low enough $B\rho$ range, so as to adequately collect the neutron-deficient fragments that are products of high-energy fission processes.

Furthermore, the dashed (green) line is the full CoMD calculation with $t_{\rm decay} = 5000$ fm/c (see Sec. III D). This line closely follows the two-step calculations CoMD/SMM and DIT/SMM for the hot fragments. In other words, the complete CoMD calculations result in fission fragments that are nearly

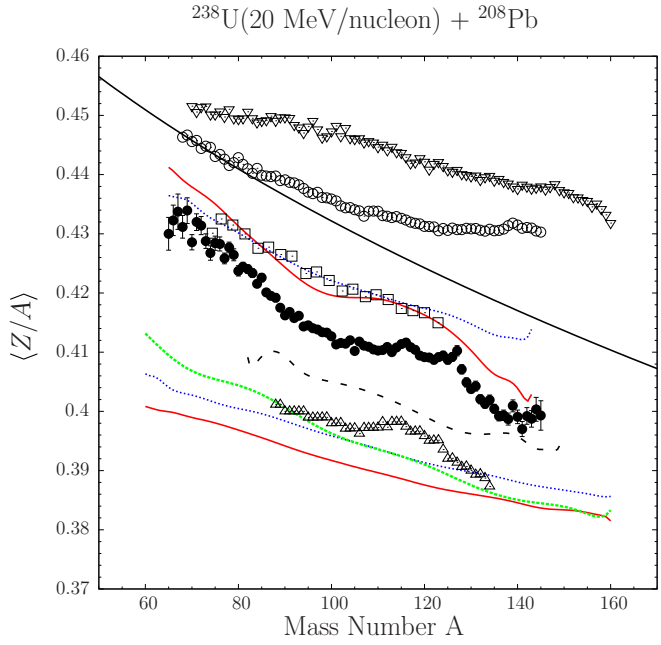

FIG. 2. Average Z/A vs A of projectile fission fragments from the reaction ^{238}U (20 MeV/nucleon) + ^{208}Pb. The experimental data for U+Pb are given by the closed points [42]. The full (red) lines are calculations with DIT/SMM. The dotted (blue) lines are calculations with CoMD/SMM. The upper set of curves are the final (cold) fission fragments. The lower set of curves are the hot fission fragments (after the SMM binary partition, but before deexcitation). The dashed (green) line is the full CoMD calculation (1000 events, $t = 15\,000$ fm/c) with $t_{\rm decay} = 5000$ fm/c (see text). The open circles are data from ^{238}U (20 MeV/nucleon) + ^{27}Al [42,43]. The open triangles, squares, and inverted triangles are the GSI data from the reaction ^{238}U (750 MeV/nucleon) + ^{208}Pb for low-energy fission, high-energy fission and fragmentation products, respectively [74–76]. The dashed (black) line represents the radiochemical data of p (24 MeV) + ^{238}U [77] The continuous (black) line gives the line of β stability.

as neutron rich as the hot fragments from the partition stage of the SMM calculation. Thus, these fragments are still excited and require substantially longer time to evolve and give off the remain der of their excitation energy. Nonetheless, these observations give further support for the two-stage approach we adopted to describe the present reactions.

Along with our 20-MeV/nucleon U+Pb data and calculations, we show in Fig. 2 the data of 750-MeV/nucleon U+Pb from [74–76] obtained with the FRS separator at GSI. (We will call these data "GSI data" in the following discussion.) As described in the above references, the kinematical analysis of these data allowed separation of the observed fragments in three groups according to their production mechanism: (a) low-energy fission (dominated by Coulomb fission) presented in Fig. 2 with right triagles, (b) high-energy fission shown by squares, and (c) fragmentation (abrasion-ablation) shown by inverted triangles. From Fig. 2, we see that the low-energy fission GSI data are, as expected, very neutron rich and are close to our hot DIT/SMM (and CoMD/SMM) calculations for the 20-MeV/nucleon U+Pb reaction. The high-energy fission GSI data appear to follow our calculations for the cold fragments.

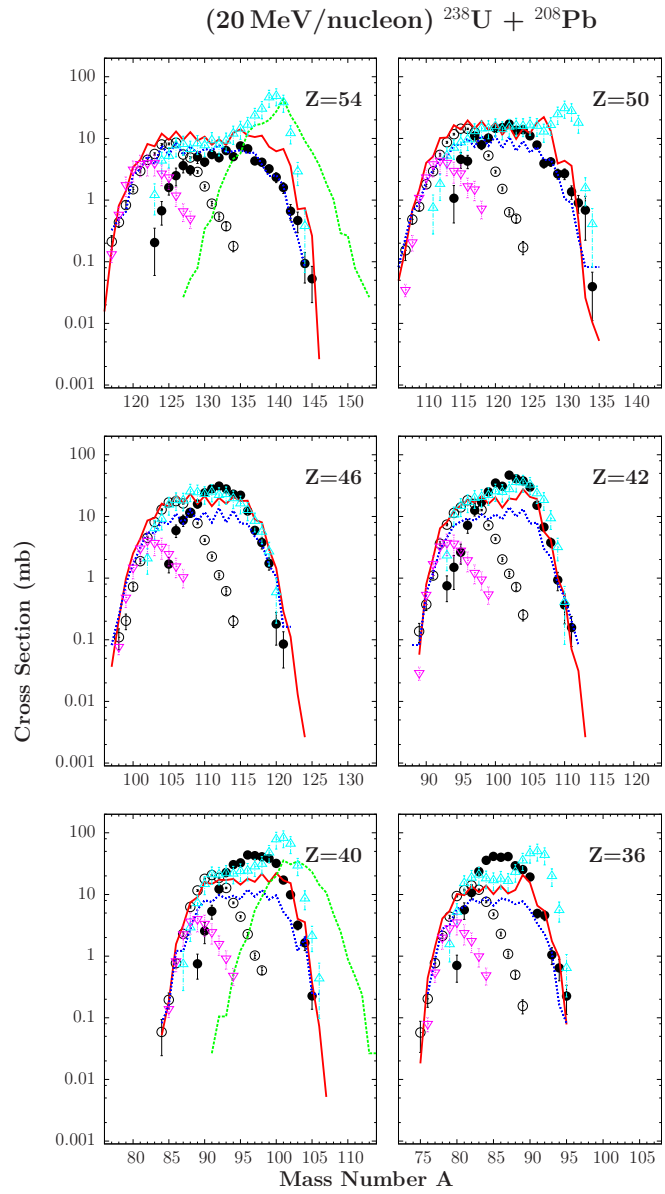

FIG. 3. Comparison of calculated mass distributions (lines) of projectile fission fragments from the reaction ^{238}U (20 MeV/nucleon) + ^{208}Pb with the experimental data (closed points) of Ref. [42]. The calculations are with DIT/SMM [solid (red) line] and with CoMD/SMM [dotted (blue) line]. The dashed (green) lines for $Z = 54$, 40 are for hot fission fragments from DIT/SMM. The open circles are data from ^{238}U (20 MeV/nucleon) + ^{27}Al [42,43]. The open right triangles and inverted triangles are the GSI data from the reaction ^{238}U (750 MeV/nucleon) + ^{208}Pb for projectile fission and fragmentation (abrasion-ablation) products, respectively [74–76].

Furthermore, the fragmentation-residue GSI data are very neutron deficient. They are more neutron deficient than our projectile fission data of ^{238}U (20 MeV/nucleon) + ^{27}Al [42,43] that we present in Fig. 2 by open circles. We briefly mention that the 20-MeV/nucleon ^{238}U + ^{27}Al data were obtained with the A1200 spectrometer under the same conditions as the U+Pb data in the magnetic rigidity range of 1.60–1.80 tesla meters (T m). This condition selected neutron-

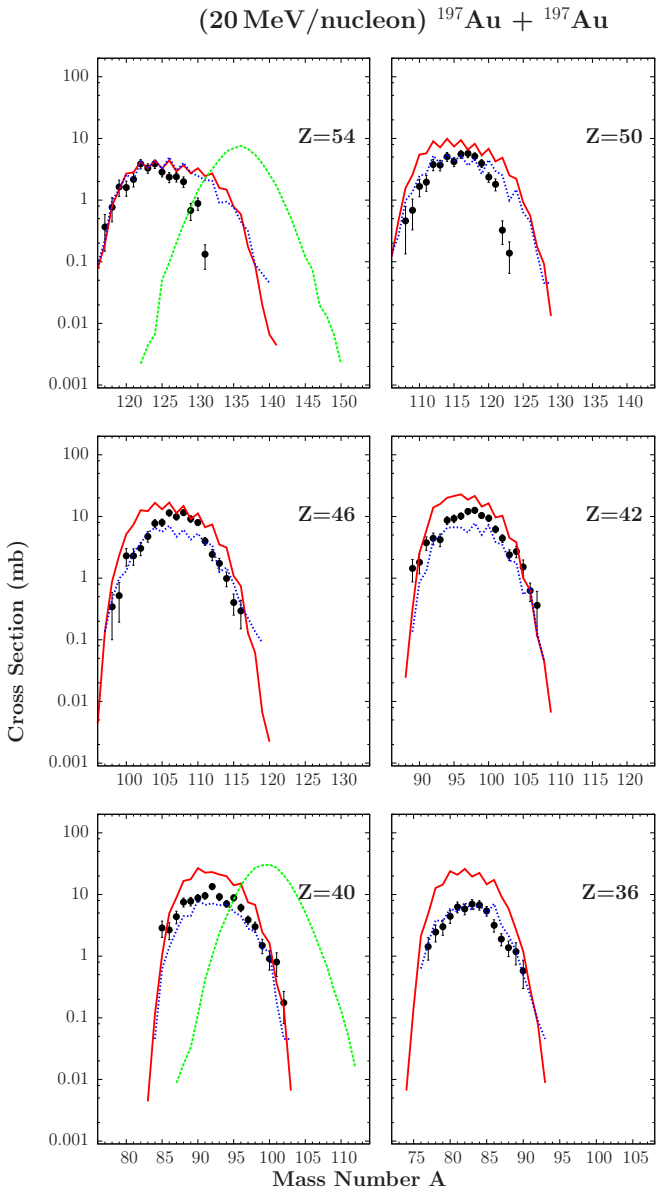

FIG. 4. Comparison of calculated mass distributions (lines) of projectile fission fragments from the reaction ^{197}Au (20 MeV/nucleon) + ^{197}Au with the experimental data (closed points) of Ref. [45]. The calculations are with DIT/SMM [solid (red) line] and with CoMD/SMM [dotted (blue) line]. The dashed (green) lines for $Z = 54, 40$ are for hot fission fragments from DIT/SMM.

deficient fission fragments coming mostly from fusionlike events. (Nuclide cross sections of these fragments are shown in Fig. 3 by open circles.) Finally, in Fig. 2, the dashed line shows the location of the radiochemical low-energy fission-fragment data of p (24 MeV) + ^{238}U [77], which are, on average, more neutron rich than our U+Pb fission-fragment data and final (cold) calculations, but less neutron rich than the GSI low-energy data.

B. Mass distributions of selected isotopes

In Fig. 3, we first present the experimental mass distributions (closed points) of several elements from the projectile fission of ^{238}U (20 MeV/nucleon) interacting with the ^{208}Pb target [42]. The DIT/SMM calculations are given by the solid (red) lines and the CoMD/SMM calculations by the dotted (blue) lines. These two calculations are close to each other on the neutron-rich side, while the latter calculations are systematically lower in the central region of the distributions (as we also observed in Fig. 1). From the figure, we observe some agreement in the shape of the calculations with the experimental cross sections. More specifically, we are able to obtain a relatively good description of the neutron-rich sides of the isotope distributions, which are of primary interest for the present work. For the neutron-deficient sides, the present calculations extend more to the left compared to the experimental data. We explored this issue in detail and concluded that in the experimental data, the magnetic rigidity range did not extend to the low-$B\rho$ region necessary for these isotopes, as we mentioned before in relation to Fig. 2.

From a practical standpoint, we infer that, in order to avoid such issues in upcoming experiments, careful consideration should be given to the necessary $B\rho$ coverage that is predictable with the help of the present model framework. We note that, along with the U+Pb calculations, we performed detailed calculations for projectile fission fragments from (20 MeV/nucleon) ^{238}U + ^{64}Ni. The U+Ni fission-fragment cross sections are very close to those of the U+Pb reaction and, for clarity, are not shown in Fig. 3, but are presented in Fig. 7 of Appendix A. Nonetheless, the angular distributions are narrower (as discussed later in relation to Fig. 5) rendering the use of the lighter target preferable for applications to neutron-rich RIB production. Moreover, in Fig. 3 the dashed green lines (for $Z = 54, 40$) show the distributions of the hot fission fragments from the DIT/SMM calculation (after the SMM partition, but before de-excitation). As we discussed before, these products are very neutron rich and de-excite toward more stable nuclides.

In Fig. 3, we also present the fission fragment data of ^{238}U (20 MeV/nucleon) + ^{27}Al (open points) which, as we discussed in relation to Fig. 2, are comprised of neutron-deficient nuclides. These data appear to complement the left side of the U+Pb data. They also seem to follow closely the left side of the DIT/SMM and CoMD/SMM calculations, implying their origin in high-energy fission processes. Interestingly, the nuclides on the left sides of the ^{238}U + ^{27}Al fission-fragment distributions extend to very proton-rich nuclei toward the proton dripline, thus rendering such a reaction a possible pathway to access proton-rich nuclides. Detailed calculations for this reaction, comparison with the data, as well as possible consideration for proton-rich RIB production are currently under way.

Finally, in Fig. 3 we present the GSI data for ^{238}U (750 MeV/nucleon) + ^{208}Pb as follows: (a) the fission fragment data coming from both low-energy and high-energy fission are shown by right triangles and (b) the fragmentation (abrasion-ablation) residue data are shown by inverted triangles and appear to follow the left side of our U+Al fission fragment data. As discussed in detail in Ref. [76], the fission-fragment cross sections of the GSI data for the neutron-rich nuclides in the region of asymmetric low-energy fission

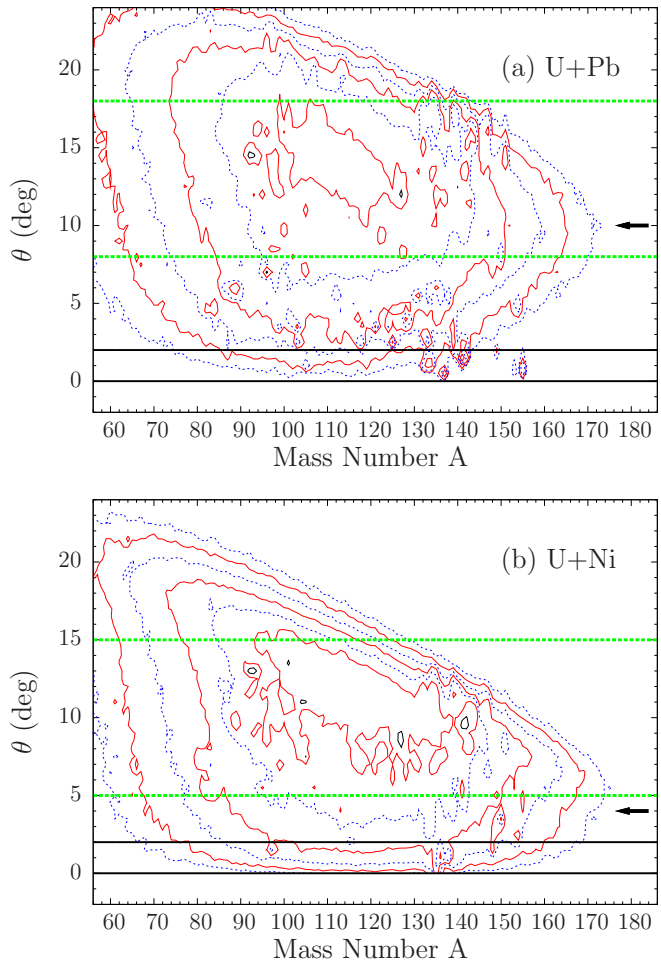

FIG. 5. (a) DIT/SMM calculated mass-resolved angular distributions of projectile fission fragments from the reaction ^{238}U (20 MeV/nucleon) + ^{208}Pb. The successive contours (starting from the innermost) represent a drop in the yield by a factor of two. The horizontal lines represent the polar angular acceptance of the A1200 spectrometer setup [42] (lower solid lines) and the KOBRA spectrometer [78] (upper dashed lines) (see text). The arrow indicates the grazing angle of the U+Pb reaction (in the laboratory system). (b) As in panel (a), but for the reaction ^{238}U (20 MeV/nucleon) + ^{64}Ni (see text).

are especially large due to the prevalence of electromagnetic fission (Coulomb fission). These cross sections (as shown for $Z = 54$, 50, 40, and 36 in Fig. 3) are larger than the 20-MeV/nucleon U+Pb data on the right side of the distributions. However, in the region of symmetric mass division they are lower and are comparable to our data for U+Pb, as seen for $Z = 46$, 42 in Fig. 3. Nevertheless, it is interesting to note that the nuclide cross sections of our U+Pb data and the GSI data are comparable near the end of the neutron-rich sides in the full range of the measured fission fragments. At this point we emphasize that the production of the most neutron-rich fragments in the relativistic U+Pb reaction comes from low-E^* (mostly Coulomb-induced) fission of the ^{238}U projectile, whereas in the 20-MeV/nucleon U+Pb reaction, it comes from fission of low-E^* U-like quasiprojectiles after nucleon exchange with the target. Thus, the lower-energy regime of 20 MeV/nucleon (or lower) may offer the opportunity to go further in neutron richness by exploiting the fission of quasiprojectiles at the high N/Z and low E^* tails of their distributions. Consequently, projectile fission at energies below the Fermi energy can be a competitive means for very neutron-rich RIB production at low-energy facilities offering intense ^{238}U beams.

In Fig. 4, we turn our attention to the projectile fission of ^{197}Au (20 MeV/nucleon) interacting with a ^{197}Au target. As we already mentioned, this reaction was studied as part of our extended study of Au-induced reactions at NSCL/MSU [44,45]. The Au+Au data were recently fully analyzed for the purpose of the present work. The general behavior of the data in comparison to our calculations is similar to that of U+Pb (as discussed in Figs 1 and 2); we thus show here only the yield distributions of several fission fragments. In Fig. 4, the experimental mass distributions are shown by full points. We see some disagreement between the data and the DIT/SMM calculations [full (red) lines] and the CoMD/SMM calculations [dotted (blue) lines] at the neutron-rich side for the heavier fission fragments ($Z = 54$, 50 in the figure). We attribute these discrepancies, in part, to incomplete $B\rho$ coverage during the experimental measurements [45]. For the lower elements, we observe that the CoMD/SMM calculations are in good agreement with the data, whereas the DIT/SMM calculations are higher than the data. The differences between the calculations may be due to differences in the excitation energy distributions of the primary quasiprojectiles predicted by the two different dynamical codes. Moreover, in Fig. 4 the dashed green lines (for $Z = 54$, 40) show the distributions of the hot fission fragments from the DIT/SMM calculation (after the SMM partition, but before de-excitation). As also seen in Fig. 3 for U+Pb, these fragments are very neutron rich and de-excite toward less exotic nuclides. Finally, we note that the beam of ^{197}Au ($N/Z = 2.49$) is not the optimum choice for the production of neutron-rich isotopes in projectile fission, compared, of course, to the ^{238}U ($N/Z = 2.59$) beam. Nevertheless, the Au+Au data offer additional detailed testing of our model framework.

In closing this section on projectile fission-fragment cross sections, we wish to briefly comment on a possible energy dependence of them. As we discuss in Appendix A, calculations for the U+Ni reaction at 10 MeV/nucleon showed nearly similar cross sections (albeit somewhat lower in the region of symmetric mass division $A = 110$–120). Moreover, calculations at 30 MeV/nucleon resulted in cross sections nearly identical to those at 20 MeV/nucleon.

C. Angular distributions

To understand the kinematics and the angular spread of the fission fragments from the projectile fission of ^{238}U at 20 MeV/nucleon, in Fig. 5(a) we show the DIT/SMM calculated mass-resolved angular distributions for U+Pb. The successive contours (starting from the innermost) represent a drop in the yield by a factor of two. The (lower) horizontal full lines represent the polar angular acceptance of the A1200 spectrometer in the experimental setup of Ref. [42] (Sec. II). The (upper) horizontal dashed lines indicate the angular

acceptance of the KOBRA separator [78], which we consider as a representative large acceptance separator appropriate for rare isotope production at this energy regime. In the KOBRA setup, we assume that the beam hits the primary target at an angle of 6° (that may be achieved with the aid of an appropriate beam swinger system [78]) and fragments are collected in the polar angular range of 8–18°. From the figure, we visually comprehend the issue of the very small acceptance of our setup in the original A1200 separator scheme. A fraction on the order of 1% or smaller of the produced projectile fission fragments falls in the angular acceptance of the A1200 spectrometer, as is also indicated quantitatively in Fig. 1. However, with an advanced large-acceptance separator like KOBRA, a substantial fraction of the projectile-fission fragments (that can reach 30–50%) can be collected, provided that we swing the primary beam at an appropriate angle (that we can choose to be near the grazing angle of the reaction).

In Fig. 5(b), we show the mass resolved angular distributions for the reaction of ^{238}U (20 MeV/nucleon) with the lighter target of ^{64}Ni. The grazing angle for this system is $\sim 4.0°$, much smaller than the U+Pb system at 20 MeV/nucleon. We clearly see that the angular distributions of the projectile fission fragments are narrower, allowing, of course, more efficient collection by the separator. For this reaction, we may assume that the beam hits the primary target at an angle of 3° in the KOBRA setup and fragments are collected in the polar angular range of 5–15°.

We note that our original choice of ^{208}Pb ($N/Z = 1.54$) as a target [42] was based on its large N/Z. However, with our present reaction model framework, we find that the calculated production cross sections of neutron-rich projectile fission fragments using the ligher ^{64}Ni ($N/Z = 1.29$) target are nearly similar to those coming from reaction using the more neutron-rich ^{208}Pb target (see Fig. 7 in Appendix A). As we discussed in the previous section, this is mainly due to the fact that the most neutron-rich fission fragments come from rather cold quasiprojectiles that, in turn, originate from peripheral collisions of the ^{238}U projectile with the targets. Because of this, we may expect only a small effect in the absolute cross sections that we wish to investigate in further detail both theoretically and experimentally. However, from a practical standpoint, the use of lighter targets is preferable, as it leads to narrower angular distributions and thus larger collection efficiency, which is desirable for applications of projectile fission in RIB production schemes. We mention that our event-by-event simulations may allow full event tracking of the products through the beam-optical elements of the separator. We can thus determine rates for the production and separation of desired neutron-rich projectile fission fragments, as is now being performed by members of the KOBRA team [78].

D. Production cross sections and rates of accessible neutron-rich nuclides

After the above discussion on production cross sections and angular distributions, we wish to provide an overall perspective of accessible neutron-rich nuclides in ^{238}U projectile fission

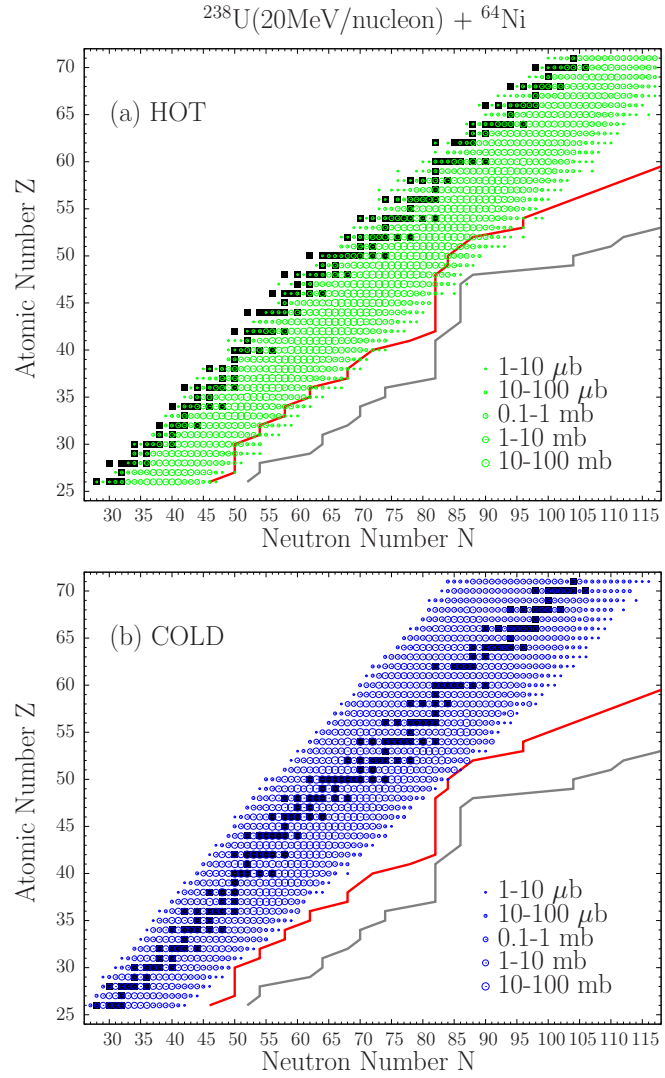

FIG. 6. Representation of DIT/SMM calculated cross sections of projectile fission fragments from the reaction ^{238}U (20 MeV/nucleon) + ^{64}Ni on the Z-N plane. The cross-sectional ranges are shown by open circles according to the key. Panel (a) shows the hot fission fragments (before de-excitation). Panel (b) shows the final (cold) fission fragments. The closed squares are the stable isotopes. The solid (red) line shows the astrophysical r-process path and the dotted (gray) line shows the location of the neutron drip-line according to Ref. [66].

at 20 MeV/nucleon. In Fig. 6(b) we show the DIT/SMM calculated production cross sections of projectile fission fragments from the reaction ^{238}U (20 MeV/nucleon) + ^{64}Ni on the Z-N plane. Several cross-sectional ranges are shown by open circles according to the figure key. The closed squares show the stable isotopes. The solid (red) line shows the astrophysical r-process path and the dashed (gray) line indicates the location of the neutron dripline as calculated by Ref. [66]. We observe that a broad range of very neutron-rich nuclides above Fe ($Z = 26$) becomes accessible with the projectile fission approach at this energy regime. Apart from the observable (cold) fission fragments [Fig. 6(b)], we show in Fig. 6(a) the hot fission fragments produced at the

partition stage of SMM. As expected, these hot fragments are extremely neutron rich and extend toward the r-process path and the neutron dripline. These isotopes are, in principle, not accessible experimentally. However, some of their properties may be inferred from detailed calculations (see, e.g., Ref. [79] and references therein). Furthermore, from an experimental point of view, kinematical reconstruction of these hot products may be possible by taking advantage of modern neutron and/or parcticle multidetectors (see, e.g., Ref. [80] and references therein).

From a practical standpoint, it is interesting to evaluate, using the above cross-sectional calculations, what total rates are expected for very short-lived neutron-rich nuclei. For this purpose, we assume a primary ^{238}U beam intensity of 10 particle nA (6.2×10^{10} particles/s) at 20 MeV/nucleon from, e.g, the RISP accelerator complex [14]. Furthermore, we assume a production target thickness of 20 mg/cm^2 ^{64}Ni, a separator angular acceptence of 20 msr, and momentum acceptance of 5%. Under these conditions, we estimate that a production cross section of 10 μb corresponds to a production rate of about 5 counts/s. Of course, the overall transmission of the separator has to be carefully taken into account along with the above estimate of total rates. However, we may conclude that for a large number of very neutron-rich nuclei, production rates of 10–1000 counts/s (at energies around 20 MeV/nucleon) are possible, allowing the study of the structure of these nuclei.

Furthermore, we point out that for very neutron-rich nuclei toward the r-process path, the predicted half-lives are less than 1 s, making their production in an ISOL facility very difficult. For such nuclei, counting rates of 10–1000 per day should be reachable with the present projectile fission approach, which suffices to verify their stability and in the most favorable cases allows measurements of their decay properties. Finally, an interesting observation from Fig. 6 is the possibility to move close to (or even reach) the neutron dripline in the region $Z = 45$–50 ($A = 130$–140) with the present projectile-fission approach.

E. Discussion and plans

We would like to conclude first with some comments on the model approaches used in this work. Starting from the full microscopic CoMD approach, we think that the overall successful description of the reaction is especially valuable due to the predictive power of the microscopic many-body approach, as we have also seen in our recent works [37,50] that does not depend on *ad hoc* assumptions of the reaction dynamics. However, the full CoMD description is very computer intensive and not practical, but essentially validates the two-step approach, as we saw in this work. As a next step, the two-stage CoMD/SMM approach provided very good results, but is still somewhat computer intensive (due to the CoMD stage of the calculation). Finally, the phenomenological DIT/SMM approach, offering results similar to the CoMD/SMM approach, is fast and, thus, can be practical for the design of experiments based on projectile fission at this energy.

In the near future, apart from further calculational efforts, we plan to perform detailed measurements of projectile fission of ^{238}U at 10–15 MeV/nucleon (a) at Texas A&M with the MARS recoil separator [11,36] and (b) at LNS/INFN with the MAGNEX large-acceptance spectrometer [81]. We expect that these measurements will provide a detailed testing ground for our models and will offer access to very neutron-rich nuclei for decay studies. Furthermore, these efforts will provide experience and preparation for future plans at upcoming large-acceptance separator facilities (e.g., KOBRA [78]). In closing, we believe that the possibility of producing very neutron-rich nuclides from projectile fission at low-energy facilities may allow a rich and diversified program of nuclear structure studies of neutron-rich rare isotopes in these facilities, complementary to the current successful programs of higher-energy RIB facilities [6,8,9].

V. CONCLUSIONS

Summarizing, we investigated the possibilities of producing neutron-rich nuclides in projectile fission of heavy beams in the energy of 20 MeV/nucleon. We reported our efforts to theoretically describe the reaction mechanism of projectile fission following a peripheral collision at this energy regime. Our calculations are mainly based on a two-step approach: The dynamical stage of the collision is described with either the phenomenological deep-inelastic transfer model (DIT) or with the microscopic constrained molecular dynamics model (CoMD). The de-excitation or fission of the hot heavy projectile fragments was performed with the statistical multifragmentation model (SMM) with appropriate settings of its parameters. We also employed the CoMD model for the full description of the reaction. We compared our model calculations with our previous experimental projectile-fission data of ^{238}U (20 MeV/nucleon) + ^{208}Pb and ^{197}Au (20 MeV/nucleon) + ^{197}Au and found an overall reasonable agreement. Our study suggests that projectile fission following peripheral heavy-ion collisions at this energy range (i.e., well above the Coulomb barrier, but below the Fermi energy) offers an effective route to access very neutron-rich rare isotopes toward the astrophysical r-process path and possibly the neutron dripline.

ACKNOWLEDGMENTS

We are thankful to Dr. L. Tassan-Got for the DIT code and to Dr. M. Papa for his version of the CoMD code. We also thank Prof. Athena Pakou for numerous enlightening discussions and suggestions. N.V. acknowledges fruitful discussions with Dr. Sato Yoshiteru. Financial support for this work was provided, in part, by the National and Kapodistrian University of Athens under ELKE Research Account No. 70/4/11395 and, in part, by the Rare Isotope Science Project of the Institute for Basic Science funded by the Ministry of Science, ICT and Future Planning, and National Research Foundation of Korea. A. Botvina acknowledges the support of BMBF (Germany). M.V. was supported by the Slovak Scientific Grant Agency under Contracts No. 2/0105/11 and No. 2/0121/14 and by the Slovak Research and Development Agency under Contracts No. APVV-0177-11 and No. APVV-15-0225.

APPENDIX A: TARGET AND ENERGY DEPENDENCE OF CROSS SECTIONS

In this appendix, we compare the calculated isotope cross sections from the 20-MeV/nucleon ^{238}U + ^{208}Pb and ^{238}U + ^{64}Ni reactions. In addition, we consider the results for a lower-energy reaction, namely the 10-MeV/nucleon ^{238}U + ^{64}Ni reaction. In Fig. 7, we first present a comparison of the DIT/SMM calculated cross sections of projectile fission fragments from the 20-MeV/nucleon ^{238}U reactions with the ^{208}Pb target [solid (red) lines] and the ^{64}Ni target [dotted (blue) lines]. As an overall observation, the cross sections are similar at both the proton-rich and the neutron-rich sides of the distributions. In the middle part of the distributions they are lower for the U+Ni system, which may be due to the lower geometrical reaction cross section of this system compared to the U+Pb system.

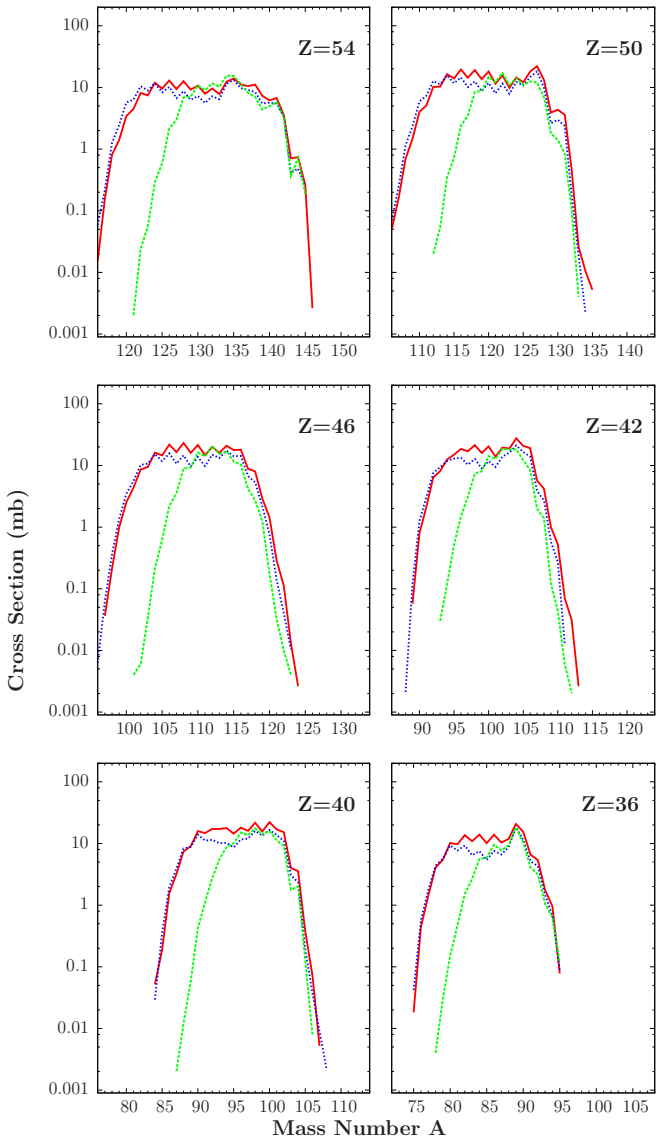

FIG. 7. Comparison of DIT/SMM calculated cross-sectional distributions of projectile fission fragments from ^{238}U induced reactions. The solid (red) lines are for the 20-MeV/nucleon ^{238}U + ^{208}Pb reaction and the dotted (blue) lines are for the 20-MeV/nucleon ^{238}U + ^{64}Ni reaction. The dashed (green) lines are for the ^{238}U + ^{64}Ni reaction at 10 MeV/nucleon.

Moreover in Fig. 7 we present the projectile fission-fragment cross sections for the U+Ni system at the lower energy of 10 MeV/nucleon. At this energy the distributions are narrower compared to those of the 20-MeV/nucleon reactions, essentially missing the proton-rich part. We may understand this as a result of the overall lower excitation energies attained in the 10-MeV/nucleon reaction that cannot lead to very proton-rich products as the 20-MeV/nucleon reactions. Furthermore, the lower-energy reaction leads to nearly similar cross sections for the neutron-rich fragment groups corresponding to asymmetric mass splits, as we observe on the neutron-rich sides of $Z = 36$ and $Z = 54$ (and, also, $Z = 40$ and $Z = 50$). On the contrary, for fragment groups corresponding to symmetric mass splits, as for $Z = 46$ and $Z = 42$, the cross sections are noticeably lower for the 10-MeV/nucleon U+Ni reaction. We do not have an explanation for this observation at present. Indeed, we would intuitively expect similar (or even higher) cross sections for the lower energy reaction. We plan to investigate the lower-energy regime of 10 MeV/nucleon (and below) in detail with both the DIT and the CoMD models in the near future. Finally, we mention that we have also performed DIT/SMM calculations for the fission fragment cross sections for the U+Ni system at 30 MeV/nucleon and the results are similar to the 20-MeV/nucleon U+Ni reaction.

APPENDIX B: PROPERTIES OF QUASIPROJECTILES

In this appendix, we delineate the main properties of the primary quasiprojectiles from the 20-MeV/nucleon ^{238}U induced reactions on ^{208}Pb and ^{64}Ni. The calculations are with the DIT model. Similar results have been obtained with the CoMD model.

In Fig. 8(a), we show the average excitation energy per nucleon E^*/A as a function of the mass A of the quasiprojectiles from the reactions U+Pb [solid (red) line] and U+Ni [dotted (blue) line]. We observe relatively low excitation energies for quasiprojectiles near ^{238}U, that, of course, correspond to a limited exchange of nucleons with the target. In contrast, substantially higher excitation energies are imparted to quasiprojectiles further away in mass from the projectile (reaching toward the nuclear multifragmentaion threshold of 3 MeV/nucleon) being higher for the U+Pb reaction than for the U+Ni reaction.

In Fig. 8(b), we show the average proton fraction Z/A as a function of the mass A of quasiprojectiles from the reactions U+Pb [solid (red) line] and U+Ni [dotted (blue) line]. The horizontal dashed line indicates the Z/A of the ^{238}U projectile. The lower and upper arrows indicate the values of fully N/Z equilibrated quasiprojectiles from the U+Pb and U+Ni reactions, respectively. The Z/A for near-projectile primary products is very close to that of the ^{238}U projectile for both reactions. For primary products further from the projectile, the Z/A departs from that of the ^{238}U projectile to values toward N/Z equilibration, especially observable for the U+Ni system [with the substantial difference between

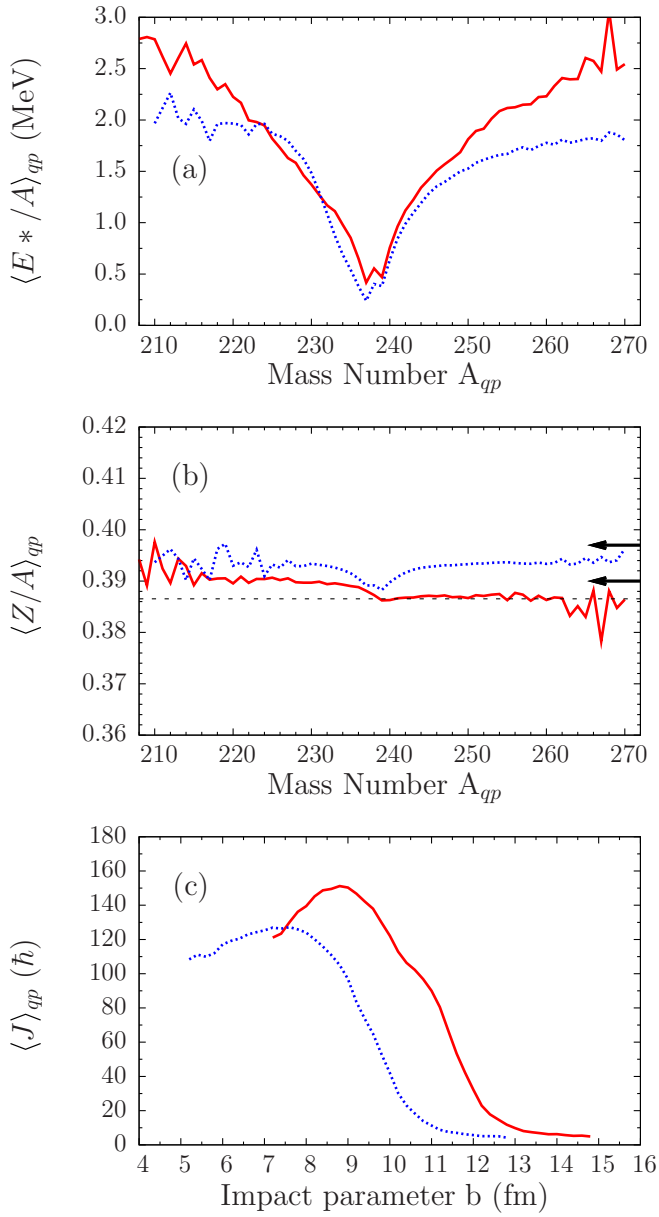

FIG. 8. DIT calculated properties of quasiprojectiles. (a) Average excitation energy per nucleon E^*/A vs mass A of quasiprojectiles from the reactions ^{238}U (20 MeV/nucleon) + ^{208}Pb [solid (red) line] and ^{238}U (20 MeV/nucleon) + ^{64}Ni [dotted (blue) line]. (b) Average Z/A vs A of quasiprojectiles. Lines are as in panel (a). The horizontal dashed line indicates the Z/A of the ^{238}U projectile. The lower and upper arrows indicate the Z/A values corresponding to full N/Z equilibration for the U+Pb and U+Ni systems, respectively. (c) Average angular momentum J of quasiprojectiles versus the impact parameter of the collision. Lines are as in panel (a).

the N/Z of ^{238}U ($N/Z = 1.59$) and ^{64}Ni ($N/Z = 1.29$) as compared to that of ^{208}Pb ($N/Z = 1.54$)].

Finally, in Fig. 8(c), we present the average angular momentum as a function of the impact parameter of the collisions U+Pb [solid (red) line] and U+Ni [dotted (blue) line]. As expected, in very peripheral collisions, low angular momenta are imparted to the reaction partners. Less peripheral collisions

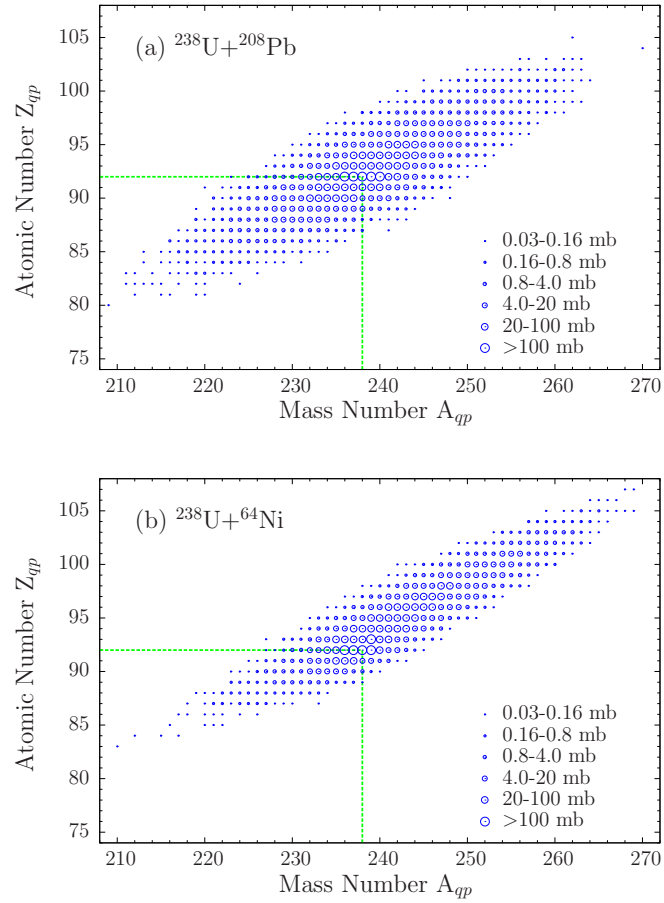

FIG. 9. Representation of DIT calculated cross sections of quasiprojectiles from the 20-MeV/nucleon reactions ^{238}U + ^{208}Pb (a) and ^{238}U + ^{64}Ni (b) on the Z-A plane. The cross-sectional ranges are shown by open circles according to the key. The lines indicate the location of the projectile nucleus ^{238}U.

lead to higher angular momenta (reaching values of 150 $\hbar$ or higher for the U+Pb system). As also indicated in the figure, the DIT calculations are terminated at 7 and 5 fm, respectively, for the U+Pb and U+Ni reactions at 20 MeV/nucleon. These values of the impact parameter correspond to interpenetration of the surfaces of the projectile and the target of approximately 3 fm, up to which point the DIT mechanism is assumed to operate (see DIT description in Sec. III A and Ref. [46]).

After the discussion of the average properties of the quasiprojectiles, we proceed with an outline of the cross-sectional distributions of these primary products. In Fig. 9, we give a representation of the DIT calculated cross sections of quasiprojectiles from the 20-MeV/nucleon reactions ^{238}U + ^{208}Pb [Fig. 9(a)] and ^{238}U + ^{64}Ni [Fig. 9(b)] on the Z-A plane. The cross section ranges are shown by open circles according to the figure key. The line segments indicate the location of the projectile nucleus ^{238}U. From these figures, we observe that the U+Pb quasiprojectile distributions are substantially wider compared to the ones from the U+Ni, whereas the latter system leads to a more extended region of transuranium elements, as compared to the U+Pb system. In

connection with Fig. 8(a), we understand that the quasiprojectiles far from the ^{238}U projectile are expected to be highly excited and decay via particle emission and/or fission (as well as multifragmentation).

[1] M. Thoennessen and B. Sherrill, Nature (London) **473**, 25 (2011).
[2] J. Erler, N. Birge, M. Kortelainen, W. Nazarewicz, E. Olsen, A. Perhac, and M. Stoitsov, Nature (London) **486**, 509 (2012).
[3] A. Gade, Eur. Phys. J. A **51**, 118 (2015).
[4] *Scientific Opportunities with a Rare-Isotope Facility in the United States* (National Academies Press, Washington, DC, 2007).
[5] D. F. Geesaman, C. K. Gelbke, R. V. F. Janssens, and B. M. Sherrill, Annu. Rev. Nucl. Part. Sci. **56**, 53 (2006).
[6] FRIB main page: www.frib.msu.edu.
[7] GANIL main page: www.ganil.fr.
[8] GSI main page: www.gsi.de.
[9] RIBF main page: www.rarf.riken.go.jp/Eng/facilities/RIBF.html.
[10] ATLAS main page: www.phy.anl.gov/atlas/facility/index.html.
[11] Texas A and M Cyclotron Institute main page: cyclotron.tamu.edu.
[12] EURISOL main page: www.eurisol.org.
[13] K.-H. Schmidt, A. Kelić, S. Lukić, M. V. Ricciardi, and M. Veselsky, Phys. Rev. ST, Accel. Beams **10**, 014701 (2007).
[14] RISP main page: www.risp.re.kr/eng/pMainPage.do.
[15] K. Tshoo *et al.*, Nucl. Instrum. Methods Phys. Res. B **317**, 242 (2013).
[16] Y. Blumenfeld, T. Nilsson, and P. V. Duppen, Phys. Scr. T **152**, 014023 (2013).
[17] A. Kelić, M. V. Ricciardi, and K. H. Schmidt, Bulg. Nucl. Soc. Trans. **13**, 98 (2009).
[18] J. C. David, Eur. Phys. J. A **51**, 68 (2015).
[19] H. Alvarez-Pol *et al.*, Phys. Rev. C **82**, 041602 (2010).
[20] J. Kurcewicz *et al.*, Phys. Lett. B **717**, 371 (2012).
[21] H. Watanabe *et al.*, Phys. Rev. Lett. **111**, 152501 (2013).
[22] C. Santamaria *et al.*, Phys. Rev. Lett. **115**, 192501 (2015).
[23] O. B. Tarasov *et al.*, Phys. Rev. C **80**, 034609 (2009).
[24] S. Lukyanov *et al.*, Phys. Rev. C **80**, 014609 (2009).
[25] O. B. Tarasov *et al.*, Phys. Rev. C **87**, 054612 (2013).
[26] C. Mazzocchi *et al.*, Phys. Rev. C **88**, 064320 (2013).
[27] T. Kurtukian-Nieto *et al.*, Phys. Rev. C **89**, 024616 (2014).
[28] Z. Meisel *et al.*, Phys. Rev. C **93**, 035805 (2016).
[29] R. Caballero-Folch *et al.*, Phys. Rev. Lett. **117**, 012501 (2016).
[30] G. G. Adamian, N. V. Antonenko, S. M. Lukyanov, and Y. E. Penionzhkevich, Phys. Rev. C **78**, 024613 (2008).
[31] V. V. Volkov, Phys. Rep. **44**, 93 (1978).
[32] L. Corradi, G. Pollarolo, and S. Szilner, J. Phys. G **36**, 113101 (2009).
[33] Y. X. Watanabe *et al.*, Phys. Rev. Lett. **115**, 172503 (2015).
[34] J. S. Barrett *et al.*, Phys. Rev. C **91**, 064615 (2015).
[35] N. Wang and L. Guo, Phys. Lett. B **760**, 236 (2016).
[36] G. A. Souliotis, M. Veselsky, S. Galanopoulos, M. Jandel, Z. Kohley, L. W. May, D. V. Shetty, B. C. Stein, and S. J. Yennello, Phys. Rev. C **84**, 064607 (2011).
[37] P. N. Fountas, G. A. Souliotis, M. Veselsky, and A. Bonasera, Phys. Rev. C **90**, 064613 (2014).
[38] G. A. Souliotis *et al.*, Phys. Lett. B **543**, 163 (2002).
[39] G. A. Souliotis, M. Veselsky, G. Chubarian, L. Trache, A. Keksis, E. Martin, D. V. Shetty, and S. J. Yennello, Phys. Rev. Lett. **91**, 022701 (2003).
[40] G. A. Souliotis *et al.*, Nucl. Instrum. Methods Phys. Res. B **204**, 166 (2003).
[41] G. A. Souliotis *et al.*, Nucl. Instrum. Methods Phys. Res. B **266**, 4692 (2008).
[42] G. A. Souliotis, W. Lovel and, K. E. Zyromski, G. J. Wozniak, D. J. Morrissey, J. O. Liljenzin, and K. Aleklett, Phys. Rev. C **55**, R2146(R) (1997).
[43] G. A. Souliotis *et al.*, in *Proceedings of the Second International Conference on Fission and Properties of Neutron-Rich Nuclides, St. Andrews, Scotland, UK, June 1999* (World Scientific, London, UK, 2000), p. 478.
[44] G. A. Souliotis, G. A. Souliotis, K. Hanold, W. Lovel and, I. Lhenry, D. J. Morrissey, A. C. Veeck, and G. J. Wozniak, Phys. Rev. C **57**, 3129 (1998).
[45] G. A. Souliotis *et al.*, Nucl. Phys. A **705**, 279 (2002).
[46] L. Tassan-Got and C. Stefan, Nucl. Phys. A **524**, 121 (1991).
[47] M. Papa, T. Maruyama, and A. Bonasera, Phys. Rev. C **64**, 024612 (2001).
[48] J. Bondorf *et al.*, Phys. Rep. **257**, 133 (1995).
[49] A. S. Botvina and I. N. Mishustin, Phys. Rev. C **63**, 061601 (2001).
[50] N. Vonta, G. A. Souliotis, M. Veselsky, and A. Bonasera, Phys. Rev. C **92**, 024616 (2015).
[51] B. M. Sherrill, D. J. Morrissey, J. A. Nolen Jr., and J. A. Winger, Nucl. Instrum. Meth. Phys. Res. B **56–57**, 1106 (1991).
[52] D. Swan, J. Yurkon, and D. J. Morrissey, Nucl. Instrum. Methods Phys. Res. A **348**, 314 (1994).
[53] F. Hubert, R. Bimbot, and H. Gauvin, At. Data Nucl. Data Tables **46**, 1 (1990).
[54] F. Hubert, R. Bimbot, and H. Gauvin, Nucl. Instrum. Methods B **36**, 357 (1989).
[55] A. Leon *et al.*, At. Data Nucl. Data Tables **69**, 217 (1998).
[56] W. W. Wilcke *et al.*, At. Data Nucl. Data Tables **25**, 389 (1980).
[57] M. Veselsky, R. W. Ibbotson, R. Laforest, E. Ramakrishnan, D. J. Rowl and, A. Ruangma, E. M. Winchester, E. Martin, and S. J. Yennello, Phys. Rev. C **62**, 064613 (2000).
[58] M. Veselsky *et al.*, Nucl. Phys. A **705**, 193 (2002).
[59] M. Veselsky *et al.*, Nucl. Phys. A **724**, 431 (2003).
[60] A. L. Keksis *et al.*, Phys. Rev. C **81**, 054602 (2010).
[61] G. A. Souliotis *et al.*, Phys. Rev. C **90**, 064612 (2014).
[62] M. Veselsky and G. A. Souliotis, Nucl. Phys. A **872**, 1 (2011).
[63] M. Papa *et al.*, J. Comp. Phys. **208**, 403 (2005).
[64] J. Aichelin, Phys. Rep. **202**, 233 (1991).
[65] M. Papa, Phys. Rev. C **87**, 014001 (2013).
[66] P. Moller, J. R. Nix, and K. L. Kratz, At. Data Nucl. Data Tables **66**, 131 (1997).
[67] N. Buyukcizmeci, R. Ogul, and A. S. Botvina, Eur. Phys. J. A **25**, 57 (2005).
[68] G. A. Souliotis, A. S. Botvina, D. V. Shetty, A. L. Keksis, M. Jandel, M. Veselsky, and S. J. Yennello, Phys. Rev. C **75**, 011601 (2007).

[69] N. Eren, N. Buyukcizmeci, R. Ogul, and A. S. Botvina, Eur. Phys. J. A **49**, 48 (2013).
[70] N. Bohr and J. A. Wheeler, Phys. Rev. **56**, 426 (1939).
[71] W. D. Myers and W. J. Swiatecki, Nucl. Phys. **81**, 1 (1966).
[72] A. S. Iljinov *et al.*, Nucl. Phys. A **543**, 517 (1992).
[73] U. Brosa, S. Grossman, and A. Muller, Phys. Rep. **167**, 1990 (2001).
[74] T. Enqvist *et al.*, Nucl. Phys. A **658**, 47 (1999).
[75] W. Schwab *et al.*, Eur. Phys. J. A **2**, 179 (1998).
[76] C. Donzaud *et al.*, Eur. Phys. J. A **1**, 407 (1998).
[77] H. Kudo, M. Maruyama, M. Tanikawa, T. Shinozuka, and M. Fujioka, Phys. Rev. C **57**, 178 (1998).
[78] K. Tshoo *et al.*, Nucl. Instrum. Methods Phys. Res. B **376**, 188 (2016).
[79] H. Imal, A. Ergun, N. Buyukcizmeci, R. Ogul, A. S. Botvina, and W. Trautmann, Phys. Rev. C **91**, 034605 (2015).
[80] W. Lin *et al.*, Phys. Rev. C **90**, 044603 (2014).
[81] F. Cappuzzello, C. Agodi, D. Carbone, and M. Cavallaro, Eur. Phys. J. A **52**, 167 (2016).